



HAL
open science

Link between stochastic grid perturbation and location uncertainty framework

Simon Clement, Eric Blayo, Laurent Debreu, Jean-Michel Brankart, Pierre Brasseur, Long Li, Etienne Mémin

► To cite this version:

Simon Clement, Eric Blayo, Laurent Debreu, Jean-Michel Brankart, Pierre Brasseur, et al.. Link between stochastic grid perturbation and location uncertainty framework. 2024. hal-04629335v2

HAL Id: hal-04629335

<https://inria.hal.science/hal-04629335v2>

Preprint submitted on 17 Jan 2025

HAL is a multi-disciplinary open access archive for the deposit and dissemination of scientific research documents, whether they are published or not. The documents may come from teaching and research institutions in France or abroad, or from public or private research centers.

L'archive ouverte pluridisciplinaire **HAL**, est destinée au dépôt et à la diffusion de documents scientifiques de niveau recherche, publiés ou non, émanant des établissements d'enseignement et de recherche français ou étrangers, des laboratoires publics ou privés.



Distributed under a Creative Commons Attribution 4.0 International License

Link between stochastic grid perturbation and location uncertainty framework

S. Clément¹, E. Blayo¹, L. Debreu¹, J-M. Brankart², P. Brasseur², L. Li³, E. Mémin³

¹Univ. Grenoble Alpes, Inria, CNRS, Grenoble INP, LJK, Grenoble, France

²Univ. Grenoble Alpes, CNRS, IRD, Grenoble INP, IGE, Grenoble, France

³Univ. Rennes, Inria, IRMAR, Rennes, France

Key Points:

- A rapidly moving grid can be a valid implementation of the Location Uncertainty (LU) framework in the absence of stochastic forcing
- Correlated noise in time and a compensating advection term are introduced to preserve both LU properties and structure of the original grid
- A statistical analysis highlights the importance of the compensation term in the implementation of the method

Corresponding author: Eric Blayo, eric.blayo@univ-grenoble-alpes.fr

15 **Abstract**

16 This paper investigates the relationship between a Stochastic Grid Perturbation (SGP)
 17 and Location Uncertainty (LU) in the context of ocean modeling. The LU formulation,
 18 which introduces random velocity fluctuations, has shown efficacy in organizing large-scale
 19 flow and replicating long-term statistical characteristics. SGP was created as a simpler
 20 approach which perturbs the computational grid for ensemble members, aiming to simulate
 21 small uncertainties in high-resolution predictability studies. We aim to clarify the link
 22 between SGP and LU. After introducing the LU formalism, we derive the SGP method and
 23 discuss its connection to LU. Correlated noise in time is introduced in the SGP method
 24 to preserve the structure of the original grid. A compensating advection term is shown to
 25 preserve LU properties despite the latter correlated noise. Numerical experiments on a 3-
 26 layer Quasi-Geostrophic model compare various SGP implementations with an explicit LU
 27 implementation, highlighting the importance of the compensating advection term to achieve
 28 strict equivalence.

29 **Plain Language Summary**

30 This paper examines two subgrid stochastic parameterizations to improve ocean and
 31 climate predictions: Stochastic Grid Perturbation (SGP) and Location Uncertainty (LU).

32 LU is a general framework for deriving stochastic representations of fluid dynamics.
 33 It decomposes the Lagrangian velocity into a smooth-in-time resolved component and an
 34 unresolved random component that is smooth in space but white in time. The LU dynamics
 35 enables the representation of large-scale patterns while preserving important physical prop-
 36 erties, such as energy balance. It also incorporates the statistical effects associated with the
 37 inhomogeneity of unresolved small-scale dynamics.

38 In a more empirical way, SGP slightly shifts the positions of grid points in numerical
 39 models to study the impact of small uncertainties in ocean forecasts, originally used for
 40 high-resolution studies of specific regions.

41 We explore the relationship between SGP and LU, finding that SGP can be adjusted to
 42 work similarly to LU. Through computer simulations, we validate our findings and examine
 43 some consequences of the possible discrepancies between the theoretical LU method and the
 44 practical SGP method. Understanding the link between SGP and LU can lead to better
 45 description of uncertainties in ocean models, and thus to improved forecasts. Our goal is to
 46 make advanced techniques like LU more accessible for broader scientific use.

47 **1 Introduction**

48 The need for uncertainty quantification in designing probabilistic simulations, con-
 49 structing plausible scenarios in climate modeling, and developing efficient ensemble meth-
 50 ods for data assimilation supports the adoption of stochastic parameterization in geophys-
 51 ical flow models. Starting with classical subgrid modeling, parameterizations with energy
 52 backscattering ability and stochastic perturbation have long been proposed (Leith, 1990;
 53 Mason & Thomson, 1992). These techniques, notably based on Markovian quasi-Gaussian
 54 closures (Kraichnan, 1959) and expressed in the spectral domain, have been successfully
 55 explored for the theoretical study of turbulence (Lesieur & Métais, 1996). These ideas of
 56 stochastic perturbations have been further developed in climate modeling (see the reviews
 57 Berner et al. (2017); Gottwald et al. (2017); Kitsios et al. (2023); O’Kane et al. (2023) and
 58 references therein, as well as the seminal work of Hasselmann (1976)). Most of the models
 59 studied in these works, however, are built on empirical grounds and lack generality. Unlike
 60 deterministic models, they are not derived through a general methodology that respects
 61 classical physical invariants. They are conceived by considering additional stochastic forc-
 62 ing, perturbation of the parameters, or semi empirical fast-slow scale decomposition. As a

63 result, they may face issues such as uncontrolled variance growth if not compensated for
 64 by additional dissipation terms. Additionally, for very low noise levels, they may deviate
 65 strongly from the associated underlying deterministic system (Chapron et al., 2018).

66 To avoid such inconsistency, ensure good physical and mathematical properties, and
 67 guarantee numerical stability, it is crucial to derive these stochastic representations using
 68 a rigorous framework. Along this path, two companion methodologies, based on stochastic
 69 transport and time decorrelation assumption, have been introduced by Mémín (2014) and
 70 Holm (2015), providing rigorously justified approaches to defining stochastic large-scale flow
 71 representations (Crisan et al., 2019; Debussche et al., 2023), conserving energy and circula-
 72 tion, respectively. The first method, which is energy-preserving and referred to as modeling
 73 under Location Uncertainty (LU), is a Newtonian framework, while the second is a varia-
 74 tional framework. As in the deterministic setting, these two approaches are complementary.
 75 In this work, we will focus exclusively on the first methodology.

76 LU has proven to be versatile in developing various models, ranging from reduced-order
 77 models (Chapron et al., 2018) and quasi-geostrophic models (Li et al., 2023a) to wave models
 78 (Mémín et al., 2024) and stochastic primitive hydrostatic models (Tucciarone et al., 2023).
 79 These models have been shown to be efficient in organizing large-scale flow (Bauer et al.,
 80 2020a) and replicating long-term statistical characteristics (Bauer et al., 2020b; Li et al.,
 81 2023a) within barotropic and baroclinic quasi-geostrophic models. Due to its construction,
 82 based on a stochastic representation of the Reynolds transport theorem, LU models ex-
 83 hibit the same theoretical energy conservation properties as the corresponding deterministic
 84 models (e.g., energy or tracer moments) (Brecht et al., 2021; Li et al., 2023a; Resseguier
 85 et al., 2017a). They also maintain key theoretical convergence properties (Debussche et
 86 al., 2023; Lang et al., 2023), when expressed and understood in a stochastic sense. These
 87 desirable theoretical results for LU models stem from an intrinsic balance between variance
 88 production and dissipation. The formulation naturally incorporates in its core (through
 89 stochastic transport) a direct expression of the fluctuation-dissipation theorem, maintaining
 90 theoretically a strict equilibrium between the energy introduced by the noise and the energy
 91 dissipated by the system (Bauer et al., 2020a; Resseguier et al., 2017a). Moreover, the
 92 convergence to deterministic equations as noise vanishes (Chapron et al., 2018; Debussche
 93 et al., 2023) ensures physical consistency in large-scale representation. It is worth noting
 94 that such convergence is not trivial, especially for non-Gaussian multiplicative noise; ad hoc
 95 noise, at the vanishing limit (i.e., for very small, but non zero, noise), may exhibit different
 96 attractors or velocity increment probability distributions (see for instance Chapron et al.
 97 (2018) for an example in the Lorenz 63 system). It is desirable for the system to behave
 98 consistently with the underlying deterministic dynamics when noise is minimal.

99 However, even though stochastic equations are increasingly recommended for subgrid
 100 parameterizations and ensemble simulations, the perceived difficulty of understanding and
 101 implementing them remains a barrier to widespread adoption.

102 Using another point of view, Leroux et al. (2022) propose a method called here “Stochas-
 103 tic Grid Perturbation” (SGP) to control the covariance of their ensemble by rapidly per-
 104 turbing the computational grid for each ensemble member. The aim is to simulate a small
 105 uncertainty in the numerical model in order to study its impact as part of a very high-
 106 resolution predictability study of the Western Mediterranean. This method resembles the
 107 Location Uncertainty formalism, where the position of the points fluctuate randomly.

108 In a data assimilation context, Zhen et al. (2023) replaced the inflation step by the
 109 application of an uncorrelated-in-time transport map (i.e. the state variables are modified
 110 along a displacement in the underlying coordinates). They formally find links to the LU
 111 framework and to the stochastic advection by Lie transport proposed by Holm (2015). Since
 112 remapping the physical space is analogous to perturbing the grid points, this may indicate
 113 a connection between “Stochastic Grid Perturbation” and the LU approach.

114 In this paper, we present a first attempt to clarify this link between SGP and LU
 115 and discuss the benefits of such Lagrangian parameterization. The LU formalism is first
 116 introduced in Section 2. The derivation of the SGP method is then discussed in Section
 117 3 with a link to the LU formalism. Numerical experiments are carried out to compare
 118 several SGP implementations with an explicit LU implementation in Section 4. Finally, the
 119 link between LU and SGP is summarized in Section 5 together with a discussion on the
 120 application scenarios of SGP.

121 2 Equations of fluids under Location Uncertainty

122 This section presents the main points of the derivation of the Location Uncertainty
 123 framework. A more explicit derivation can be found in Bauer et al. (2020a) and Resseguier
 124 et al. (2017a). The notations and properties are presented in a concise way in §2.1, and §2.2
 125 details the derivation which will be linked to the Stochastic Grid Perturbation method.

126 2.1 Location Uncertainty formalism

127 The central hypothesis of the LU framework is the identification of two scales of motion:
 128 similarly to a Reynolds averaging, the evolution of the position of a particle \mathbf{X}_t has a large-
 129 scale contribution which is smooth and explicitly resolved and a small-scale unresolved
 130 component that is assumed uncorrelated in time at the characteristic time scale of the
 131 resolved component, and referred to as “noise”:

$$132 \quad d\mathbf{X}_t = \underbrace{\mathbf{v}(\mathbf{X}_t, t)dt}_{\text{Large scale motion}} + \underbrace{\sigma(\mathbf{X}_t, t)d\mathbf{B}_t}_{\text{Small scale uncertainty}} \quad (1)$$

133 The cylindrical Brownian motion $\mathbf{B}_t(\mathbf{x})$ is uncorrelated in time but correlated in space.
 134 Notably, the idealized assumption of temporal decorrelation makes it possible, by means of
 135 stochastic calculus, to explicitly take into account the correlation terms between the resolved
 136 and unresolved components, which are usually added afterward (e.g. large-scale diffusion,
 137 bolus velocity, modified advection...). In particular, this allows to explain in a different way
 138 certain models proposed in a fully deterministic framework (see for instance the relations
 139 with the Craik-Leibovich system for Langmuir turbulence (Bauer et al., 2020a)). Note
 140 that the resolved velocity component is also a stochastic process – i.e. unlike the Reynolds
 141 average decomposition it is not an expectation.

142 The absence of time correlation can be seen as the assumption that the characteristic
 143 time scale of turbulence is much smaller than the time step of the numerical model. This
 144 simplification of the true continuum of spatial and temporal scales of turbulence assumes
 145 that turbulent fluctuations rapidly decorrelate within each time step, allowing them to
 146 be treated as independent from one step to the next. In this sense LU can be seen as an
 147 expression of the dynamics in the temporal decorrelation limit of the small scales (Debussche
 148 & Mémin, 2024). The spatial correlation of the noise is enforced through the operator
 149 $\sigma(\mathbf{X}_t, t)$. The latter is a Hilbert-Schmidt integral operator and can thus be defined through
 150 a kernel $\check{\sigma}$:

$$151 \quad \sigma(\mathbf{X}_t, t)d\mathbf{B}_t \triangleq \int_{\Omega} \check{\sigma}(\mathbf{X}_t, \mathbf{y}, t)d\mathbf{B}_t(\mathbf{y})d\mathbf{y}.$$

152 At this point, we need to make several comments on our notations:

- 153 • bold letters indicate that the values are in \mathbb{R}^2 . \mathbf{B}_t has hence two components and the
- 154 kernel $\check{\sigma}$ is a 2×2 matrix.
- 155 • The computational domain Ω is a bounded domain of \mathbb{R}^2 .
- 156 • The differential notation used in (1) actually represents the equality between the in-
- 157 tegrated terms $\mathbf{X}_t - \mathbf{X}_0 = \int_0^t \mathbf{v}dt + \int_0^t \sigma d\mathbf{B}_t$ where the last integral is a Itô stochastic
- 158 integral. The Itô integral is a martingale of null ensemble mean, which is why it
- 159 is preferred to the Stratonovich integral in most settings based on LU. Despite the

160 martingale property, the noise features a non-zero mean component through the intro-
 161 duction of a Girsanov drift (see Li et al., 2023b): it consists in a change of probability
 162 measure and resembles a smooth transport term.

163 Finally, if q is a quantity such that $dq = 0$ (i.e. $q(\mathbf{X}_{t+\delta t}, t + \delta t) = q(\mathbf{X}_t, t)$) one can use the
 164 stochastic calculus tools to obtain the definition of the *stochastic transport operator*:

$$165 \quad \mathbb{D}_t q \triangleq d_t q + (\mathbf{v}^* dt + \sigma d\mathbf{B}_t) \cdot \nabla q - \frac{1}{2} \nabla \cdot (\mathbf{a} \nabla q) dt = 0. \quad (2)$$

166 The variance \mathbf{a} of the noise (or one-point-one-time correlation matrix) is defined by $\mathbf{a}(\mathbf{x}, t) \triangleq$
 167 $\int_{\Omega} \check{\sigma}(\mathbf{x}, \mathbf{y}, t) \check{\sigma}^T(\mathbf{x}, \mathbf{y}, t) d\mathbf{y}$. The effective velocity \mathbf{v}^* is defined by $\mathbf{v}^* \triangleq \mathbf{v} - \frac{1}{2} \nabla \cdot \mathbf{a} + \sigma^T (\nabla \cdot \sigma)$.
 168 When expressed in Stratonovich notation, the diffusion term is implicit and the transport of
 169 a passive scalar quantity corresponds to the model proposed by Kraichnan (1994), which has
 170 been extensively used for theoretical studies (Falkovich et al., 2001; Gawedzky & Kupiainen,
 171 1995; Majda & Kramer, 1999). Although based on a strong idealized decorrelation property,
 172 this model exhibits in particular anomalous dissipation.

173 The differences between the total (Lagrangian) derivative $dq \triangleq q(\mathbf{X}_{t+\delta t}, t + \delta t) - q(\mathbf{X}_t, t)$,
 174 the temporal Eulerian increment $d_t q \triangleq q(\mathbf{X}_t, t + \delta t) - q(\mathbf{X}_t, t)$ and the stochastic transport
 175 operator $\mathbb{D}_t q$ are essential. Indeed, as we will see in §3, the Stochastic Grid Perturbation
 176 method consists in connecting the first two operators and aims to simulate the last one. Let
 177 us mention that the transport operator is formally defined. As in the deterministic case, the
 178 stochastic partial differential equations (SPDEs) derived from it are only defined in a weak
 179 sense, meaning that the functions are not necessarily differentiable in a strong sense. The
 180 noise is assumed to be smooth in space (in the weak sense) while the function considered
 181 are not smoother than in the deterministic case. Interested readers may find precise math-
 182 ematical assumptions for the noise in the LU Navier-Stokes equations in (Debussche et al.,
 183 2023). It is also worth pointing out that for a linear transport equation, the type of noise
 184 we are dealing with (called transport noise) allows for relaxing the Lipschitz condition on
 185 the resolved drift (Fedrizzi & Flandoli, 2013)

186 2.2 Detailed derivation

187 This section contains the technical derivation of the stochastic transport operator \mathbb{D}_t
 188 which is crucial for the upcoming proof of the Stochastic Grid Perturbation method. Readers
 189 focused on the final results can skip this Section without losing the main thread.

190 The starting point of the LU derivation is the Ito-Wentzell formula (Kunita, 1990)
 191 which is a chain rule for random (semimartingale) functions with random (semimartingale)
 192 arguments:

193 **Ito-Wentzell formula.** *Let $f(\mathbf{x}, t)$ be a C^2 -process over $\mathbf{x} \in \mathbb{R}^d$ and C^1 -semimartingale*
 194 *over $t \in \mathbb{R}^+$; let \mathbf{X} be a semimartingale over $\Omega \subset \mathbb{R}^d$. $f(\mathbf{X}, t)$ is a semimartingale satisfying*

$$195 \quad df = d_t f + \sum_{i=1}^d \frac{\partial f}{\partial x_i} dX^i + \frac{1}{2} \sum_{i,j=1}^d \frac{\partial^2 f}{\partial x_i \partial x_j} d\langle X^i, X^j \rangle_t + \sum_{i=1}^d d\langle \frac{\partial f}{\partial x_i}(\mathbf{X}, \cdot), X^i \rangle_t \quad (3)$$

196 Applying the Ito-Wentzell formula (3) to $dq(\mathbf{X}_t, t)$ decomposes the total derivative dq
 197 into a time increment $d_t q$ (which plays the role of a partial derivative), a transport term
 198 $(v + \sigma d\mathbf{B}_t) \cdot \nabla q$ and additional quadratic co-variation terms:

$$199 \quad dq = d_t q + \sum_{i=1}^d \frac{\partial q}{\partial x_i} (\sigma d\mathbf{B}_t)^i + \frac{1}{2} \sum_{i,j=1}^d \frac{\partial^2 q}{\partial x_i \partial x_j} d\langle X^i, X^j \rangle_t + \sum_{i=1}^d d\langle \frac{\partial q}{\partial x_i}(\mathbf{X}, \cdot), X^i \rangle_t + v \cdot \nabla q dt \quad (4)$$

200 Following the derivation of Li et al. (2023a), the quadratic co-variation $d\langle X^i, X^j \rangle_t$ is equal
 201 to $a_{ij} dt$. The time increment $d_t q$ is then decomposed into its smooth component and its

202 time uncorrelated component:

$$203 \quad d_t q = f(\mathbf{X}_t, t) dt + \int_{\Omega} \sum_{k=1}^d g_k(\mathbf{X}_t, \mathbf{y}, t) d\mathbf{B}_t^k(\mathbf{y}) dy. \quad (5)$$

204 The quadratic co-variation depends only on the uncorrelated parts. The gradient of the
 205 tracer can hence be replaced by its uncorrelated component in the quadratic co-variation
 206 with the stochastic flow:

$$207 \quad \left\langle \frac{\partial q}{\partial x_i}, X^i \right\rangle_t = \int_{\Omega} \sum_{j=1}^d \check{\sigma}_{ij}(\mathbf{X}_t, \mathbf{y}, t) \frac{\partial g_j}{\partial x_i}(\mathbf{X}_t, \mathbf{y}, t) dy, \quad \forall i = 1, \dots, d \quad (6)$$

208 This leads to use the canonical decomposition of semi-martingales (i.e. the decomposition
 209 (5) is unique) to identify f and g in the equation $dq = 0$:

$$210 \quad f = -\frac{1}{2} \sum_{i,j=1}^d a_{ij} \frac{\partial^2 q}{\partial x_i \partial x_j} - \int_{\Omega} \sum_{j=1}^d \check{\sigma}_{ij}(\mathbf{X}_t, \mathbf{y}, t) \frac{\partial g_j}{\partial x_i}(\mathbf{X}_t, \mathbf{y}, t) dy - v \cdot \nabla q$$

$$211 \quad g_j = -\sum_{k=1}^d \check{\sigma}_{jk} \frac{\partial q}{\partial x_k}.$$

211 This identification specifies $d_t q$ for a tracer conserved by the flow. It depends notably on
 212 the quadratic co-variation (6) which can be further expanded with the substitution of g_j .
 213 After some calculus, one obtains

$$214 \quad \int_{\Omega} \check{\sigma}_{ij} \frac{\partial g_j}{\partial x_i} = -\underbrace{\frac{1}{2} a_{ik} \frac{\partial^2 q}{\partial x_i \partial x_k}}_{\text{cancelled (in } f)} - \underbrace{\frac{1}{2} \frac{\partial}{\partial x_i} \left(a_{ik} \frac{\partial q}{\partial x_k} \right)}_{\nabla \cdot (a \nabla q)} - \underbrace{\frac{1}{2} \frac{\partial a_{ik}}{\partial x_i} \frac{\partial q}{\partial x_k} + \sigma_{jk} \frac{\sigma_{ij}}{\partial x_i} \frac{\partial q}{\partial x_k}}_{(v^* - v) \cdot \nabla q} \quad (8)$$

215 where the summation are dropped for sake of simplicity. By replacing f and g in (5), one
 216 obtains the definition of the stochastic transport operator (2):

$$217 \quad \mathbb{D}_t q \triangleq d_t q + (v^* dt + \sigma d\mathbf{B}_t) \cdot \nabla q - \frac{1}{2} \nabla \cdot (a \nabla q) dt = 0.$$

218 This derivation was based on the assumption $dq = 0$ but it can be extended to other
 219 equations involving dq (e.g. Resseguier et al., 2017b).

220 3 Stochastic Grid Perturbation

221 Let us consider a Finite Difference space discretization where the grid points are noted
 222 \mathbf{x}_i , i being a space index. The Stochastic Grid Perturbation method consists in moving grid
 223 points in a Lagrangian manner following the small scale uncertainty (see Figure 1). The
 224 continuous formulation in time reads:

$$225 \quad \mathbf{x}_i^{\text{Brownian}}(t) - \mathbf{x}_i(0) = \int_0^t (\sigma d\mathbf{B}_t)_i \quad (9)$$

226 This method is illustrated in §3.1 with the simple example of a transport equation and is
 227 compared with the Location Uncertainty (LU) framework. Then §3.2 presents how time
 228 correlation in the grid motion (to keep the structure of the grid) can be compensated by
 229 an additional advection term. The exact link between the Stochastic Grid Perturbation
 230 method and Location Uncertainty is then discussed in §3.3.

231 3.1 Transport equation on a perturbed grid

232 We first show the effect of using the SGP method on the transport equation $\partial_t q dt =$
 233 $-\mathbf{v} \nabla q dt$. The left-hand side loses its time differentiability and becomes

$$234 \quad q(\mathbf{x}_i^{\text{Brownian}}(t + \delta t), t + \delta t) - q(\mathbf{x}_i^{\text{Brownian}}(t), t).$$

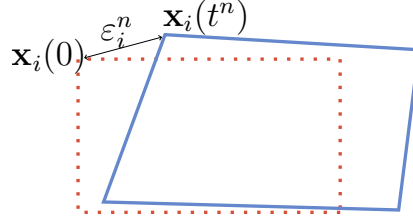


Figure 1. Illustration of the grid perturbation: dotted lines represent the initial grid and solid lines represent the perturbed grid at time t^n . All points are drifted to the right in order to illustrate the fact that the noise is spatially correlated.

- 235 • In the particular case where $\mathbf{v} = 0$, one can recognize a Lagrangian discretization of
 236 a cancelling total derivative $dq = 0$. The total derivative and the presence of noise
 237 is at the heart of the LU framework. Following step by step the derivation of the
 238 stochastic transport operator in §2.2 with $\mathbf{v} = 0$, the Ito-Wentzell formula applied
 239 to $q(\mathbf{x}_i^{\text{Brownian}}(t + \delta t), t + \delta t) - q(\mathbf{x}_i^{\text{Brownian}}(t), t)$ yields the right-hand side of (4)
 240 which contains a time increment $d_t q$, the perturbation term $\sigma d\mathbf{B}_t \cdot \nabla q$ and additional
 241 co-variation terms. Using the canonical martingale decomposition (5) of the time
 242 increment and exploiting its uniqueness to identify smooth and uncorrelated terms
 243 leads to (7), using (6) to simplify the smooth parts. With the slight simplification
 244 that $v = 0$, the expansion of the quadratic covariation (8) finally gives

$$245 \begin{cases} d\mathbf{x}_i^{\text{Brownian}} &= (\sigma d\mathbf{B}_t)_i \\ dq(\mathbf{x}_i, t) &= 0 \end{cases} \implies \mathbb{D}_t q = 0, \quad (\mathbf{v} = 0) \quad (10)$$

- 246 • In the general case with any \mathbf{v} , the left-hand side can be noted $d_t(q \circ \mathbf{x}_i^{\text{Brownian}})$ (where
 247 \circ is the composition) and represents a material derivative taking only the uncorrelated
 248 part of the velocity into account (see §3.3). The derivation of §2.2 can still be followed
 249 by applying the Ito-Wentzell formula (3) on $d_t(q \circ \mathbf{x}_i^{\text{Brownian}}, t) + v \cdot \nabla q dt$ which gives the
 250 right-hand side of (4). The canonical decomposition of semimartingales is then used
 251 on the equation $d_t(q \circ \mathbf{x}_i^{\text{Brownian}}, t) = -v \cdot \nabla q dt$, which yields system (7). Assuming a
 252 perfect discretization of ∇q , one finally obtains

$$253 \begin{cases} d\mathbf{x}_i^{\text{Brownian}} &= (\sigma d\mathbf{B}_t)_i \\ d_t(q \circ \mathbf{x}_i^{\text{Brownian}}) &= -\mathbf{v}(\mathbf{x}_i, t) \cdot \nabla q dt \end{cases} \implies \mathbb{D}_t q = 0 \quad (11)$$

254 For the transport equation, the perturbed grid ($\mathbf{x}_i^{\text{Brownian}}$) hence implements the stochastic
 255 transport operator \mathbb{D}_t defined in (2).

256 However, $\int_0^t \sigma d\mathbf{B}_t$ is not bounded and the distance between a grid point $\mathbf{x}_i^{\text{Brownian}}(t)$
 257 and its original location $\mathbf{x}_i^{\text{Brownian}}(0)$ possibly increases infinitely. As consequences, the grid
 258 loses its structure with time and the evaluation of ∇q potentially reduces its accuracy. Two
 259 solutions can be applied to keep the grid close to its original disposition:

- 260 • Restore the grid to its original state by interpolating all the variables. However, this
 261 global interpolation has a significant cost. It is interesting to note that in the particu-
 262 lar case of some semi-Lagrangian models, an interpolation is already implemented
 263 to realign the grid points to their original positions.
 264 • Introduce a time-correlated noise which keeps $\mathbf{x}_i(t) - \mathbf{x}_i(0)$ close to zero. This is the
 265 subject of §3.2.

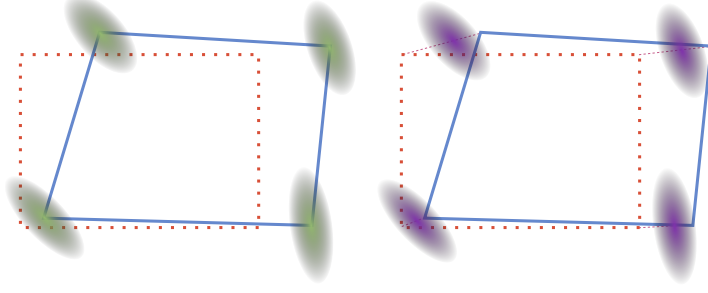


Figure 2. Representation of Brownian (left) and Auto-Regressive (right) noises for the grid perturbation. Dotted lines are the initial grid, solid lines are the current perturbed grid, and the ellipses represent the positions of the future grid points. Auto-Regressive processes perform a translation of the probability density function from the current grid towards the initial grid.

3.2 Ornstein-Uhlenbeck processes in Stochastic Grid Perturbation

In their grid perturbation, Leroux et al. (2022) did not use a Brownian motion but an auto-regressive process. The crucial property of auto-regressive processes is that it is possible to bound their variance, which removes the problem of grid divergence mentioned earlier. Let us note the current perturbation of a grid point $\varepsilon_i^n = \mathbf{x}_i(t_n) - \mathbf{x}_i(0)$ as in Figure 1. The first order Auto-Regressive process AR(1) is

$$\varepsilon_i^n = e^{-\alpha\delta t}\varepsilon_i^{n-1} + \sigma(\mathbf{B}(t_n) - \mathbf{B}(t_{n-1})) \quad (12)$$

where $e^{-\alpha\delta t}$ is slightly smaller than 1 to ensure that the variance of AR(1) is bounded for $n \rightarrow \infty$. The continuous counterparts of AR(1) are Ornstein-Uhlenbeck processes R_t , which satisfy the stochastic differential equation

$$d\mathbf{R}_t = -\alpha\mathbf{R}_t dt + \sigma d\mathbf{B}_t, \quad R_0 = 0. \quad (13)$$

Injecting equation (13) in (11) yields

$$\begin{cases} d\mathbf{x}_i^{\text{Brownian}} &= \alpha\mathbf{R}_t dt + d\mathbf{R}_t \\ d_t(q \circ \mathbf{x}_i^{\text{Brownian}}) &= -\mathbf{v}(\mathbf{x}_i, t) \cdot \nabla q dt \end{cases} \implies \mathbb{D}_t q = 0 \quad (14)$$

Similarly to §3.1, the nudging term $\alpha\mathbf{R}_t dt$ can be “transferred” from the first line to the second line of the system. The effect is to change the noise of the perturbation and to compensate this change by an additional advection term which depends on the current displacement of the grid:

$$\begin{cases} d\mathbf{x}_i^{\text{O-U}} &= d\mathbf{R}_t \\ d_t(q \circ \mathbf{x}_i^{\text{O-U}}) &= (-\mathbf{v}(\mathbf{x}_i, t) + \alpha\mathbf{R}_t) \cdot \nabla q dt \end{cases} \implies \mathbb{D}_t q = 0 \quad (15)$$

Figure 2 represents the difference between Brownian and Auto-Regressive processes in the Stochastic Grid Perturbation method. It should be noted that the probability density function is simply translated towards the initial grid in the second case.

Remark. In a discrete-in-time setting, the AR(1) process can replace Ornstein-Uhlenbeck process in the previous operations and the compensation can be derived at the discrete level. One then obtains

$$\underbrace{\sigma(\mathbf{B}(t_n) - \mathbf{B}(t_{n-1}))}_{\text{“}\sigma d\mathbf{B}_t\text{”}} = \underbrace{(\varepsilon_i^n - \varepsilon_i^{n-1})}_{\text{“}d\mathbf{R}_t\text{”}} + \underbrace{(1 - e^{-\alpha\delta t})\varepsilon_i^{n-1}}_{\text{“}\alpha\mathbf{R}_t dt\text{”}}$$

Following the continuous case, the compensation term $\alpha\mathbf{R}_t \cdot \nabla q dt$ can be discretized by $((1 - e^{-\alpha\delta t})\varepsilon_i^{n-1}) \cdot \nabla q$. It is interesting to note that the compensation uses the grid disposition at the former time step and not at the current one. The grid at the former time step must hence be stored to implement this discrete compensation term.

3.3 General link between SGP and LU

Let us define the operator ∂_t^{SGP} which represents (at the continuous level in time) a partial derivative in time under the Stochastic Grid Perturbation method: for a quantity θ , its definition is $\partial_t^{\text{SGP}}\theta \triangleq d_t(\theta \circ \mathbf{x}_i^{\text{Brownian}})$. If a Ornstein-Uhlenbeck process is used, as proposed in §3.2, in order to keep the grid close to its original state, then one can use an alternative (but equivalent) definition: $\partial_t^{\text{SGP}}\theta \triangleq d_t(\theta \circ \mathbf{x}_i^{\text{O-U}}) - \alpha \mathbf{R}_t \cdot \nabla \theta dt$. This section clarifies the links and differences between $\partial_t^{\text{SGP}}\theta$, the total variation $d\theta$ and the stochastic transport operator $\mathbb{D}_t\theta$.

Applying the Ito-Wentzell formula (3) to $\partial_t^{\text{SGP}}\theta$, one obtains:

$$\partial_t^{\text{SGP}}\theta = d_t\theta + \sum_{i=1}^d \frac{\partial\theta}{\partial x_i} (\sigma d\mathbf{B}_t)^i + \frac{1}{2} \sum_{i,j=1}^d \frac{\partial^2\theta}{\partial x_i \partial x_j} d\langle X^i, X^j \rangle_t + \sum_{i=1}^d d\left\langle \frac{\partial\theta}{\partial x_i}(\mathbf{X}, \cdot), X^i \right\rangle_t. \quad (16)$$

This operator ∂_t^{SGP} only takes into account the uncorrelated component of the velocity. The variations $d\theta$ and $\partial_t^{\text{SGP}}\theta$ (given by equations (4) and (16), respectively) differ only in the presence of a transport term by the smooth component of the velocity:

$$\partial_t^{\text{SGP}}\theta = d\theta - \mathbf{v} \cdot \nabla \theta dt. \quad (17)$$

The SGP operator is hence equivalent to the total derivative without the smooth velocity.

Note that, in (16), the last term $d\left\langle \frac{\partial\theta}{\partial x_i}(\mathbf{X}, \cdot), X^i \right\rangle_t$ depends on the equation under consideration. For instance for $\partial_t^{\text{SGP}}\theta + \mathbf{v} \cdot \nabla \theta dt = 0$, this term leads (as explained in §2.2) to $\partial_t^{\text{SGP}}\theta + \mathbf{v} \cdot \nabla \theta = \mathbb{D}_t\theta$. Conversely, the presence of a non-zero right-hand side can instigate a modification in the very definition of ∂_t^{SGP} , causing it to diverge from \mathbb{D}_t (which is defined independently of the equation). The rest of this section focuses on explaining this difference between the Stochastic Grid Perturbation and Eulerian implementations of the Location Uncertainty parameterization.

Appendix B of Resseguier et al. (2017a) derives the difference between the material derivative and the stochastic transport operator. This difference is non-zero only in the presence of a stochastic forcing. They decompose $\mathbb{D}_t\theta$ into a smooth part $f dt$ and an uncorrelated component $\mathbf{h}^T d\mathbf{B}_t$:

$$\mathbb{D}_t\theta = f dt + \mathbf{h}^T d\mathbf{B}_t. \quad (18)$$

This decomposition leads them to $d\theta = \mathbb{D}_t\theta + tr(\sigma^T \nabla \mathbf{h}^T) dt$, which gives a relation between the stochastic transport operator and the partial derivative in time under Stochastic Grid Perturbation:

$$\partial_t^{\text{SGP}}\theta + \mathbf{v} \cdot \nabla \theta dt = d\theta = \mathbb{D}_t\theta + tr(\sigma^T \nabla \mathbf{h}^T) dt. \quad (19)$$

To illustrate the importance of the term $tr(\sigma^T \nabla \mathbf{h}^T)$, let us consider the example of the Quasi-Geostrophic (QG) equations. In the numerical experiments of Section 4, the QG equations will be based on the transport of potential vorticity and feature no stochastic forcing (see §4.1). This formulation ensures that $tr(\sigma^T \nabla \mathbf{h}^T) = 0$. Conversely, in Li et al. (2023a) one can see that, when considering QG equations based on the momentum $\mathbf{u} = (u, v)$, one has $\mathbf{h}^T d\mathbf{B}_t = \beta y \mathbf{k} \times \sigma_h d\mathbf{B}_t$. More precisely,

$$\begin{pmatrix} \mathbf{h}_u^T d\mathbf{B}_t \\ \mathbf{h}_v^T d\mathbf{B}_t \end{pmatrix} = \beta y \mathbf{k} \times \sigma_h d\mathbf{B}_t = \beta y \begin{pmatrix} -(\sigma_h d\mathbf{B}_t)_y \\ (\sigma_h d\mathbf{B}_t)_x \end{pmatrix} = \beta y \begin{pmatrix} -\sigma_{21} & -\sigma_{22} \\ \sigma_{11} & \sigma_{12} \end{pmatrix} d\mathbf{B}_t.$$

This noise is additive and a simplified form of $tr(\sigma^T \nabla \mathbf{h}_u^T)$, $tr(\sigma^T \nabla \mathbf{h}_v^T)$ can be derived. The difference between $(\partial_t^{\text{SGP}}\mathbf{u} + \mathbf{v} \cdot \nabla \mathbf{u} dt)$ and $\mathbb{D}_t\mathbf{u}$ is finally

$$\begin{pmatrix} tr(\sigma^T \nabla \mathbf{h}_u^T) \\ tr(\sigma^T \nabla \mathbf{h}_v^T) \end{pmatrix} dt = \beta y \begin{pmatrix} -\sum_i \sigma_{i\bullet} \partial_i \cdot \sigma_{2\bullet} \\ \sum_i \sigma_{i\bullet} \partial_i \cdot \sigma_{1\bullet} \end{pmatrix} dt + \beta \begin{pmatrix} \sigma_{21}^2 + \sigma_{22}^2 \\ \sigma_{1\bullet} \cdot \sigma_{2\bullet} \end{pmatrix} dt, \quad (20)$$

336 where \bullet stands for any index value. Injecting the values of β, y, σ used in the numerical
 337 experiments of Section 4, we numerically obtain that $\frac{\|tr(\sigma^T \nabla \mathbf{h}^T) dt\|_\infty}{\|d\mathbf{u}\|_\infty} < 10^{-4}$ and
 338 $\frac{\|tr(\sigma^T \nabla \mathbf{h}^T) dt\|_2}{\|d\mathbf{u}\|_2} < 10^{-3}$. This suggests that the difference between SGP and LU is minimal
 339 in practice.

340 In the opposite case of systems which do not contain any stochastic forcing, the SGP
 341 is strictly equivalent to the stochastic transport operator:

$$342 \quad \partial_t^{\text{SGP}} q + \mathbf{v} \cdot \nabla q dt = \mathbb{D}_t q \quad (21)$$

343 This strict equivalence notably occurs in the equations numerically studied in the following
 344 section.

345 4 Numerical experiments

346 In this section we examine the Stochastic Grid Perturbation method applied on a 3-layer
 347 Quasi-Geostrophic model described in §4.1. Several simulations using different approaches
 348 are described in §4.2. Those simulations are compared qualitatively in §4.3 then quantitatively
 349 in §4.4.

350 4.1 Numerical model description

351 The numerical model we used was created by Thiry et al. (2023) and slightly modified
 352 to make the Stochastic Grid Perturbation possible. This model is described here again for
 353 completeness. In all the numerical experiments the prognostic variables are the potential
 354 vorticity $\mathbf{q} = \begin{bmatrix} q_1 \\ q_2 \\ q_3 \end{bmatrix}$ (in s^{-1}) and the dynamic pressure $\mathbf{p} = \begin{bmatrix} p_1 \\ p_2 \\ p_3 \end{bmatrix}$ (in $\text{m}^2 \cdot \text{s}^{-2}$), stacked in
 355 three isopycnal layers. The 3-layer QG equations read:

$$356 \quad \partial_t \mathbf{q} = \frac{1}{f_0} J(\mathbf{q}, \mathbf{p}) + f_0 B \mathbf{e} - \frac{a_4}{f_0} \Delta^2 (\Delta \mathbf{p}), \quad (22)$$

$$357 \quad (\Delta - f_0^2 A) \mathbf{p} = f_0 \mathbf{q} - f_0 \beta (y - y_0), \quad (23)$$

359 where Δ is the horizontal Laplacian, Δ^2 the biharmonic operator, $J(a, b) = \partial_x a \partial_y b - \partial_x b \partial_y a$
 360 stands for the Jacobi operator, $f_0 + \beta(y - y_0)$ is the Coriolis parameter under beta-plane
 361 approximation with the meridional axis centered on y_0 , and a_4 is the biharmonic viscosity
 362 coefficient. In the case of grid perturbation, the time derivative ∂_t in (22) is replaced
 363 by its perturbed counterpart ∂_t^{SGP} , with spatial derivatives also influenced by the grid
 364 perturbation. For the LU framework, we specifically consider a stochastic transport of \mathbf{q}
 365 (with forcing and dissipation), namely

$$366 \quad \mathbb{D}_t q = \left(f_0 B \mathbf{e} - \frac{a_4}{f_0} \Delta^2 (\Delta \mathbf{p}) \right) dt, \quad (24)$$

367 where the same kinematic relationship as in (23) applies.

368 The three-layer QG equations are integrated in a mid-latitude-centered rectangular
 369 ocean box model configuration, similar to the implementation used by Hogg et al. (2005).
 370 The ocean circulation is driven by a stationary, symmetrical wind stress at the surface
 371 and a linear Ekman stress at the bottom, generating an eastward turbulent jet featuring
 372 an idealized Gulf Stream in which spontaneous eddy production takes place. Despite its
 373 simplicity, such an idealized model is capable of producing meaningful mesoscale dynamics
 374 provided horizontal resolution is sufficiently high and viscosity is relatively low. In this
 375 paper, simulations were carried out with a horizontal resolution of 40, 10 and 5 km. The
 376 numerical model setup was further modified by Thiry et al. (2023) to make the Stochastic
 377 Grid Perturbation method possible.

L_x, L_y	Double-gyre 3-layer QG (3840 × 4800)km
H_k	(350, 750, 2900)m
$g'_{k+0.5}$	(0.025, 0.0125) ms ⁻²
δ_{ek}	2m
τ_0	2×10^{-5} m ² s ⁻¹
Simulation time	1 year
Time step	2 hours
Temporal scheme	SSRK3
a_4	5×10^{11} m ⁴ s ⁻¹
f_0	9.37×10^{-5} s ⁻¹
β	1.75×10^{-11} m ⁻¹ s ⁻¹
α	5×10^{-5} s ⁻¹

Table 1. Model parameters shared by all simulations.

378 Table 1 gives the values of the parameters shared by all simulations. The values of B
379 and \mathbf{e} , given by Thiry et al. (2023), are:

$$380 \quad B = \begin{bmatrix} \frac{1}{H_1} & \frac{-1}{H_1} & 0 & 0 \\ 0 & \frac{1}{H_2} & \frac{-1}{H_2} & 0 \\ 0 & 0 & \frac{1}{H_3} & \frac{-1}{H_3} \end{bmatrix}, \quad \mathbf{e} = \begin{bmatrix} \partial_x \tau^y - \partial_y \tau^x \\ 0 \\ 0 \\ \frac{\delta_{ek}}{2|f_0|} \Delta p_3 \end{bmatrix}, \quad \vec{\tau} = \tau_0 \begin{bmatrix} -\cos(2\pi y/L_y) \\ 0 \end{bmatrix}, \quad (25)$$

381 where τ_0 represents the surface wind magnitude, H_k is the background thickness of the k -th
382 layer and δ_{ek} is the thickness of the lower Ekman layer. The vertical stratification of this
383 model is described by the term $-f_0^2 A \mathbf{p}$ where

$$384 \quad A = \begin{bmatrix} \frac{1}{H_1 g'_{1.5}} & \frac{-1}{H_1 g'_{1.5}} & 0 \\ \frac{-1}{H_2 g'_{1.5}} & \frac{1}{H_2} \left(\frac{1}{g'_{1.5}} + \frac{1}{g'_{2.5}} \right) & \frac{-1}{H_2 g'_{2.5}} \\ 0 & \frac{-1}{H_3 g'_{2.5}} & \frac{1}{H_3 g'_{2.5}} \end{bmatrix}, \quad (26)$$

385 with $g'_{k+0.5}$ the reduced gravity defined between layers k and $k + 1$.

386 The noise $\sigma d\mathbf{B}_t$ is computed through offline analysis of high-resolution simulations
387 based on Empirical Orthogonal Functions (see Li et al., 2023b). Specifically, high-pass
388 filtering is applied to high-resolution simulation data to extract streamfunction fluctuations,
389 from which velocity fluctuations are derived and aggregated into $N = 50$ orthogonal modes
390 via the EOF procedure. The semi-martingale associated with the noise is then represented
391 as a linear combination of these modes, weighted by standard Brownian motions:

$$392 \quad \sigma(\mathbf{x}) d\mathbf{B}_t = \sum_{i < N} \sqrt{\lambda_i} \Phi_i(\mathbf{x}) d\xi_t^i + \Gamma(\mathbf{x}) dt, \quad (27)$$

393 where λ_i is the eigenvalue associated with the spatial mode Φ_i and $(d\xi_t^i)_{i < N}$ denote in-
394 dependent and identically distributed standard Brownian motions. The drift term Γ
395 is introduced through Girsanov transformation (change of probability measure), with the aim
396 of replicating the mid-latitude jet observed in the high-resolution experiment. This field
397 is concentrated in mid-latitudes and can be found in the input data of the provided code
398 (Clement & Li, 2024).

399 This choice of σ is tailored for the LU model to resemble a high-resolution simulation.
400 Consequently, if a method differs from the LU model, using the same noise parameterization
401 is likely to result in a solution that does not resemble the high-resolution simulation. This
402 discrepancy indicates a divergence from the LU model rather than an absolute measure of
403 the method's performance. In fact, it would be possible to parameterize σ specifically for
404 this method to achieve better results.

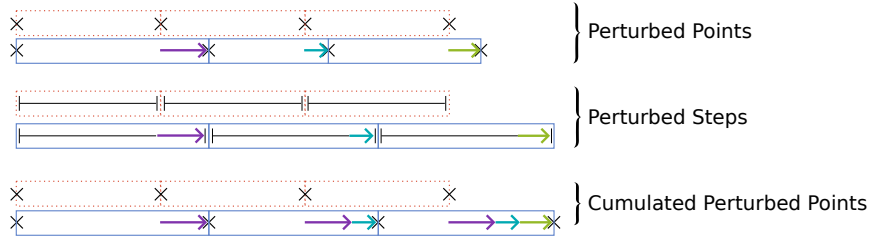


Figure 3. Illustration of the grid perturbation methods “Perturbed Points” (top) where the noise is applied to the grid points and “Perturbed Steps” (center) where the noise is applied to the space steps. The dotted orange rectangles represent the initial grid and blue rectangles represent the perturbed grid. On the bottom is an illustration of the equivalence between “Perturbed Points” with a cumulative sum of the noise and “Perturbed Steps”.

4.2 Stochastic Grid Perturbation and Metric Perturbation

The perturbation described in Leroux et al. (2022) does not consist in perturbing the grid points but instead the grid metric. The associated experiment is hence called “Perturbed Steps” and will be compared (despite its lack of direct theoretical relation with LU and its possible artefacts on the eastern boundary) to the Stochastic Grid Perturbation presented in this paper, named “Perturbed Points”. Figure 3 illustrates the difference between the two approaches. In a rectangular grid, the perturbation of the space steps amounts to modify $\sigma d\mathbf{B}_t$ with a cumulative sum from the lower space indices to the greater ones. This is illustrated on the bottom of Figure 3 where the grid points with a cumulative noise are aligned with the grid points of the “Perturbed steps” method. Inversely, moving the grid points would amount to modify the “Perturbed steps” noise by taking its difference between consecutive steps. There is hence no fundamental difference behind the distinction between “Perturbed Steps” and “Perturbed Points”. Nevertheless, we will see that the choice between the two methods significantly changes the behavior of the model if σ is kept the same.

In both cases, an Auto-Regressive process is used to preserve the structure of the grid. As it is explained in §3.2, a compensation (i.e. the additional advective term) is introduced in the “Perturbed points” method to recover the effects of an uncorrelated-in-time noise.

Remark. *The choice of the nudging intensity parameter α depends on the structure and intensity of the noise. In our numerical simulations, $\alpha = 5 \times 10^{-5} \text{ s}^{-1}$ which gives $e^{-\alpha \delta t} \approx 0.7$ for our choice of δt . The goal was to minimise α while keeping the perturbation small compared to the space step: $\epsilon_i \ll \delta x$. The value of α was chosen by hand through numerical experiments to prevent negative space steps and avoid reliance on numerical thresholds.*

To focus on the effect of the grid perturbation, the same advective term is applied to the “Perturbed steps” method. As it is illustrated on the bottom of Figure 3, the displacement of the grid points can be large in the latter method, especially with space-correlated noise. The control of the parameters of such a noise is also a difficult task because of a possible strong accumulation effect. Using this displacement to compute the compensation term leads to high advection speed which would require to drastically decrease the time step. Consequently, at the price of a possible theoretical inconsistency, the displacement of the “Perturbed points” method was used to compute the compensation, even in the “Perturbed steps” method. We consider 6 ensemble simulations (30 members each):

- Deterministic : high (10km) and low (40km) resolution
- Explicit LU

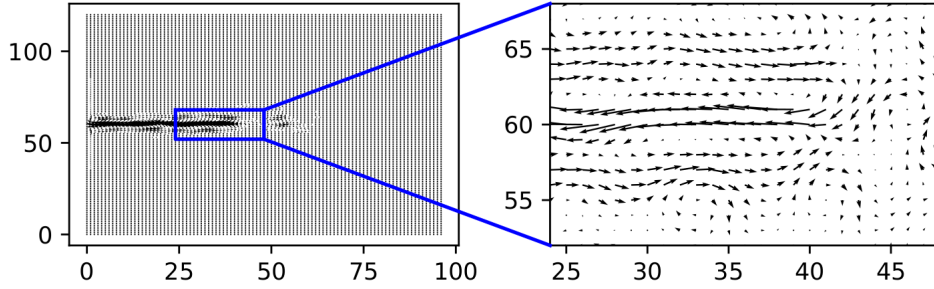


Figure 4. Visualization of the perturbation of the grid generated by the SGP method for one of the ensemble members at the end of a one-year simulation. Arrows linking the initial grid to the perturbed grid are plotted: the length of the arrows has been increased tenfold to better visualise the direction of the perturbation. On the left panel, the whole grid is represented and the right panel displays a zoom on a smaller portion.

- 439 • Perturbed Steps
- 440 • Perturbed Points
- 441 • Perturbed Points without the compensation term

442 Note that, since the role of (hyper)viscosity is to damp scales that are not properly resolved
 443 by the grid, the parameter a_4 was reduced to $10^{10} \text{ m}^4 \cdot \text{s}^{-1}$ in the high resolution simulation.
 444 Keeping this parameter constant would not significantly change the results compared to the
 445 low resolution simulation (but would require a significantly smaller time step).

446 Figure 4 shows the perturbation applied in the “Perturbed Points” case, and also serves
 447 as a representation of the noise (note that the amplitude of the perturbation is small, and
 448 that the length of the arrows has been multiplied by a factor of 10 to better visualize the
 449 displacement of the grid points). The noise features a so-called Girsanov drift to obtain a
 450 jet that is similar to the one in the deterministic High Resolution (HR) simulation (Li et
 451 al., 2023a).

452 *Creation of the initial ensemble* A very high resolution (5km, with the hyper-viscosity
 453 coefficient reduced to $a_4 = 2 \cdot 10^9 \text{ m}^4 \text{ s}^{-1}$) deterministic simulation at statistical equilibrium is
 454 used to create the initial ensemble. Assuming that the turbulence is sufficiently decorrelated
 455 in time, a snapshot of the very high resolution simulation is taken every 6 months in a 15-
 456 year simulation. To adjust the level of energy to the low resolution experiments, the (low
 457 resolution) explicit LU code then integrates in time all those snapshots for one year. For the
 458 10km-resolution deterministic experiments, the snapshots of the 5km-resolution are used
 459 directly.

460 4.3 Qualitative study

461 In this section we focus on the solution profile at the end of the one-year simulation.
 462 Recall that the LU method and “perturbed points” are theoretically the same (up to possi-
 463 bly higher-order error terms), while “perturbed steps” and “without compensation” differ
 464 at leading order. The deterministic solutions serve as references to understand how sig-
 465 nificant the differences are. For consistency, the 10 km deterministic simulation data were
 466 downsampled to the 40 km coarse grid using a low-pass filtering procedure. A Gaussian
 467 kernel with a standard deviation of $\sigma = 2$ (half of the resolution ratio) and a width of
 468 6σ (capturing 99.7% of the Gaussian distribution) was applied to filter the inner points of
 469 the high-resolution pressure fields. The boundary value of each downsampled pressure was

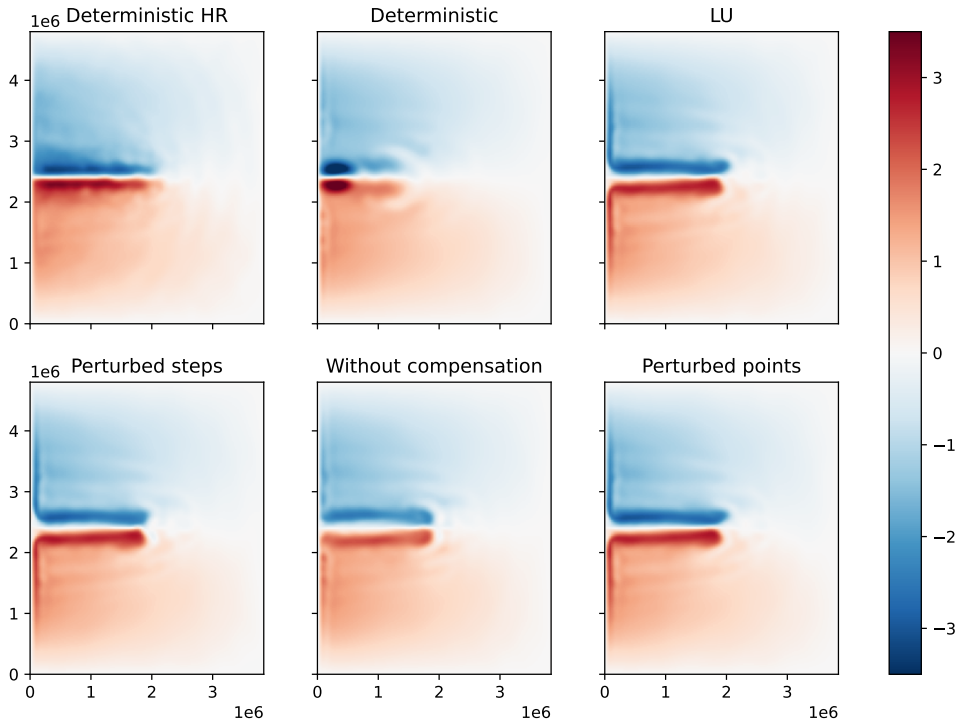


Figure 5. Surface pressure (in $\text{m}^2 \cdot \text{s}^{-2}$) averaged over the ensemble and over the last week of a one-year simulation.

470 determined by enforcing mass conservation constraints. Subsequently, other fields, such as
 471 potential vorticity, were derived on the coarse grid.

472 Figures 5 and 6 respectively present the averaged pressure and potential vorticity. The
 473 average is computed both over the ensemble and over the last week of a one-year simulation.
 474 Firstly, it can be observed that the LU formalism allows for the generation of a jet that
 475 is much more pronounced than without noise injection. The solutions of the “Perturbed
 476 Points” and “Perturbed Steps” methods do exhibit such an energetic jet: the behaviour of
 477 SGP is hence similar to LU in this regard. However, in the absence of the compensation
 478 term (experiment “Without compensation”), the jet is less pronounced.

479 Figure 7 provides the standard deviation of the surface pressure of the ensemble simu-
 480 lations. The standard deviation is also computed both over the ensemble and over the last
 481 week of the one-year simulation. It shows that, without the compensation term (“Without
 482 compensation”), the standard deviation is more concentrated at the center of the domain:
 483 it is stronger at the jet level and globally weaker in the rest of the basin. The compensa-
 484 tion term seems hence to play a crucial role in transferring ensemble variability from grid points
 485 to the state variables. Interestingly, the “Perturbed steps” simulation also seems to exhibit
 486 a higher ensemble variance at the jet level compared to the LU approach. The LU method
 487 with EOF-based noise (27) produces lower variability compared to the high-resolution de-
 488 terministic run, primarily due to the stationary assumption of the EOF approach. This
 489 limitation has been addressed in our previous works, where more advanced noise parame-
 490 terization techniques and Girsanov drift corrections, such as state-dependent projections (Li
 491 et al., 2023a) and dynamic mode decomposition (Li et al., 2023b), were shown to improve
 492 the results. However, a detailed exploration of these methods is beyond the scope of this

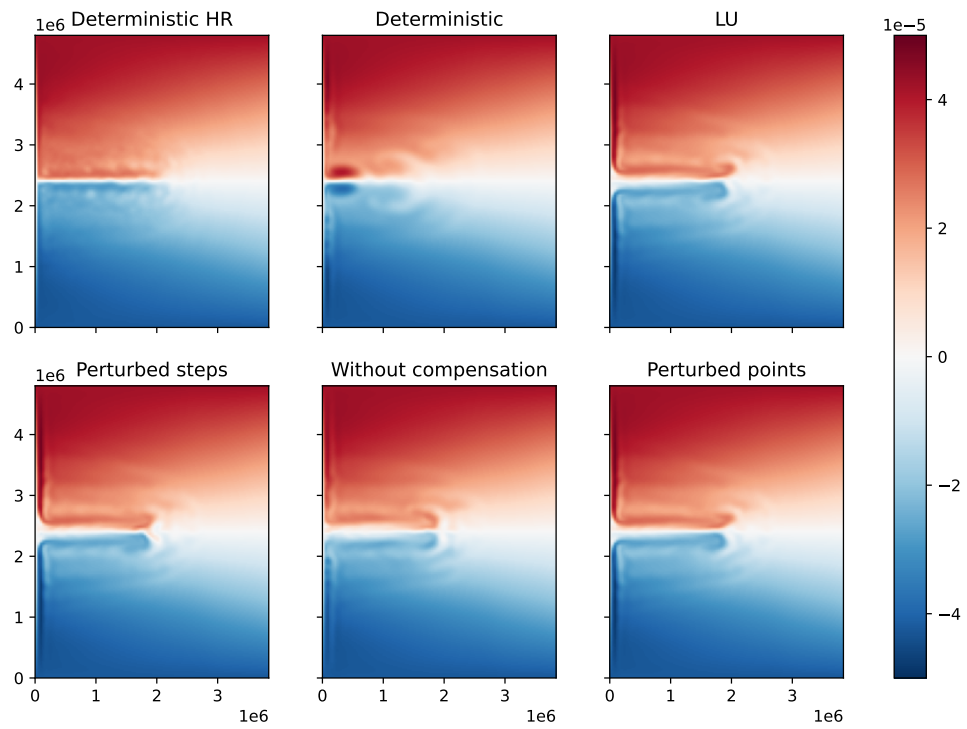


Figure 6. Surface potential vorticity (in s^{-1}) averaged over the ensemble and over the last week of a one-year simulation.

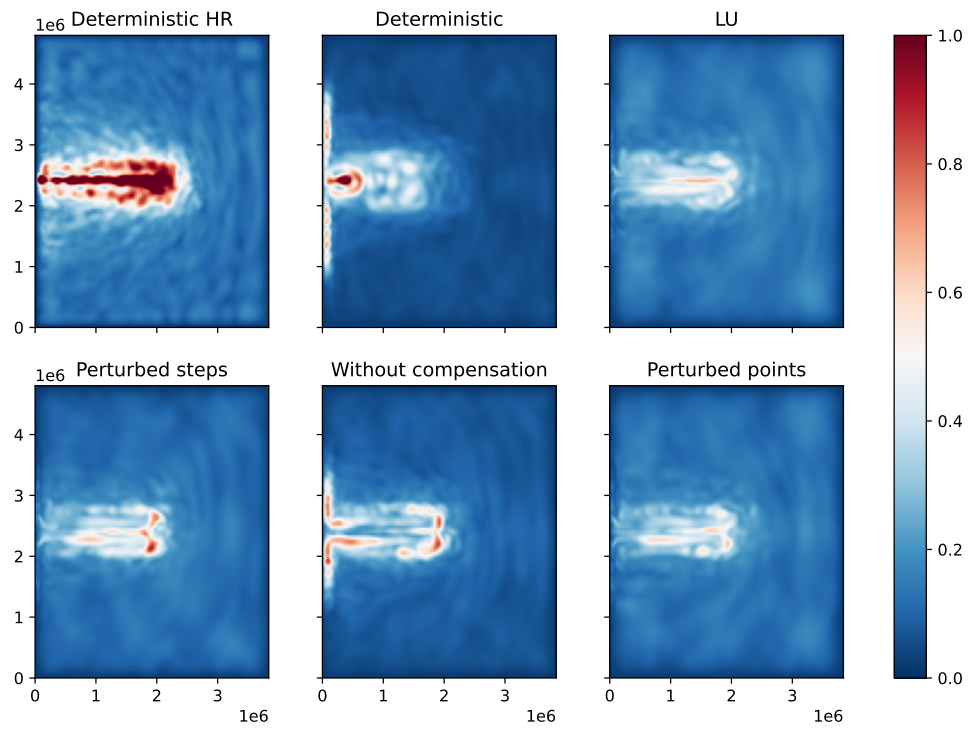


Figure 7. Point-wise standard deviation of surface pressure computed over the ensemble and over the last week of a one-year simulation.

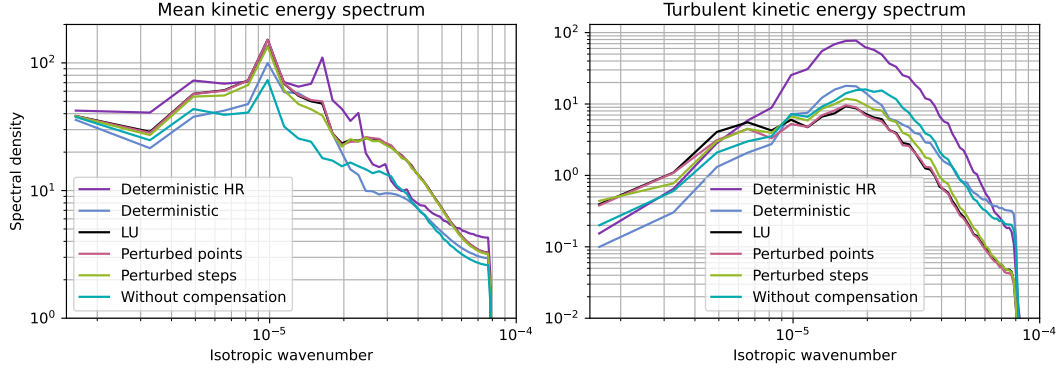


Figure 8. Mean (left) and turbulent (right) kinetic energy spectrum computed over the ensemble at the end of simulation.

493 work. The objective here is to establish the connection between grid perturbation methods
 494 and the LU framework, for which a simple yet efficient noise parameterization is sufficient to
 495 draw meaningful conclusions.

496 Figure 8 compares the mean kinetic energy (MKE) and turbulent kinetic energy (TKE)
 497 spectra of different models at the end of the simulation. The MKE spectrum reflects the en-
 498 ergy of the ensemble mean, while the TKE spectrum shows the energy of deviations within
 499 the ensemble, indicating variance across scales. The MKE spectrum reveals that both the
 500 low-resolution deterministic run and the Perturbed Points method without compensation
 501 perform poorly at large and small scales. In contrast, the LU, Perturbed Steps, and Per-
 502 turbed Points methods effectively transfer energy from small to intermediate scales, showing
 503 good backscattering. The method without compensation shows only weak backscattering
 504 and performs worse at large scales, highlighting the value of the compensation term. The
 505 TKE spectrum shows that the LU, Perturbed Points, and Perturbed Steps methods pro-
 506 duce similar results, with the correct slope and no energy buildup at the cutoff scale. The
 507 Perturbed Steps method slightly increases TKE, while the method without compensation
 508 produces higher TKE but suffers from energy accumulation at the cutoff scale. This issue
 509 highlights its weaker ability to transfer energy from fluctuations to the mean, again showing
 510 the importance of compensation.

511 4.4 Quantitative study

512 Figures 9 and 10 display the first four spatially computed standardized moments of u
 513 and q , respectively. We note $m_i(u, t) = \frac{1}{V} \int_V (u(\mathbf{x}, t) - \bar{u}(\mathbf{x}, t))^i d\mathbf{x}$ the i -th order central
 514 moment ($i \geq 2$), where V is the basin volume and $\bar{u}(\mathbf{x}, t)$ is the ensemble average of u .
 515 The standard deviation, skewness and kurtosis are respectively defined by $\sqrt{m_2}$, $\frac{m_3}{(m_2)^{1.5}}$ and
 516 $\frac{m_4}{(m_2)^2}$. One can see on those figures that the statistics of the “Perturbed points” ensemble
 517 are close to those of the “LU” ensemble. The other two methods presented approximate
 518 some statistics at the expense of others:

- 519 • The mean vorticity with the “Perturbed steps” method significantly differs from other
 520 methods. Cumulative noise from low to high indices results in stronger noise in one
 521 gyre, creating average vorticity.
 522 It was also tested to remove the compensation term in this “Perturbed steps” ex-
 523 periment: doing so also halves the creation of vorticity. The displacement of the
 524 “Perturbed points” method used to compute the compensation (see §4.1) may be a
 525 cause of creation of vorticity. However there is still an unidentified source of vorticity,

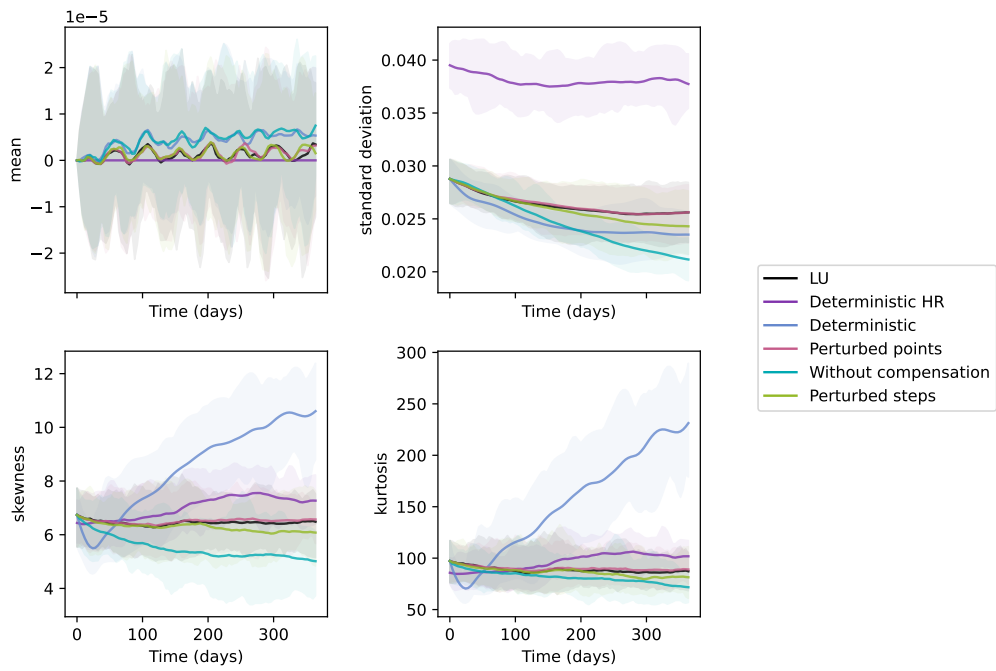


Figure 9. First four standardized moments of the variable u (reconstructed from p). Each solid line represents the average of a moment over the ensemble members, and the envelopes contain all the moment values.

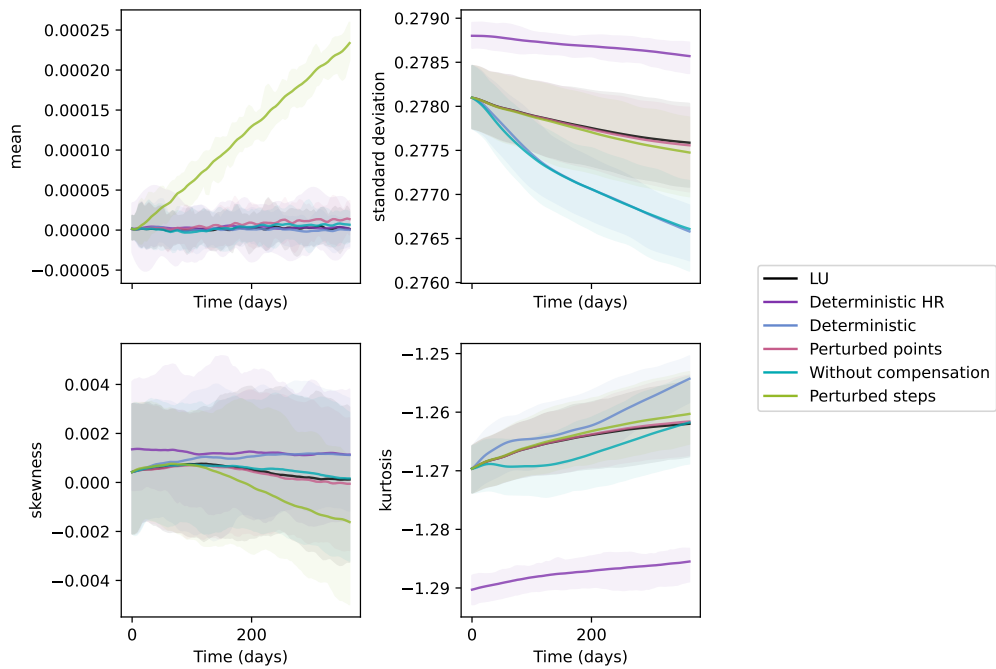


Figure 10. Same as Figure 9 but for the vorticity (variable q).

526 as removing the compensation term while using the cumulative sum in each gyre does
 527 not completely cancel the creation of vorticity.
 528 • The standard deviation for both variables is underestimated with the method “With-
 529 out compensation”. The compensation term of the “Perturbed points” method is
 530 indeed one of the keys of the transfer of variability from the grid points to the vari-
 531 ables u and q .

532 Figure 9 also features interesting characteristics of skewness and kurtosis. First, the positive
 533 skewness of the variable u suggests that extreme values are predominantly positive. The
 534 latter observation is expected, as this double-gyre configuration is characterized by the east-
 535 directed flow concentrating the extreme values. Second, the kurtosis of u in the deterministic
 536 case is much larger than in the stochastic cases, indicating more extreme values. It can be
 537 noted that the deterministic simulation appears to lead to a slightly higher variance than
 538 the simulation without compensation. This suggests that the high skewness and kurtosis of
 539 the low resolution deterministic simulation does not come from small values of the variance.
 540 Figure 6 hints that in the absence of a clear jet, the deterministic (LR) experiment may
 541 create extreme values located on the west side between the two gyres. Note that the spatial
 542 statistics of the high-resolution deterministic experiments are displayed for completeness
 543 but are difficult to compare to the low-resolution experiments.

544 An additional analysis of the moments (not shown) centered on the jet area yields
 545 the same conclusions, except that the variance, skewness and kurtosis of the low-resolution
 546 deterministic simulation are much smaller, indicating the absence of a clear jet. The creation
 547 of vorticity of the “Perturbed steps” method is also largely reduced, indicating that it does
 548 not originate from the jet.

549 Finally, these figures (for the sake of readability) only display 3 out of the 30 ensemble
 550 members. Comparing the statistics of two ensembles can be done using the Wasserstein
 551 distance. This involves finding the permutation $\pi : \llbracket 1, 30 \rrbracket \rightarrow \llbracket 1, 30 \rrbracket$ that minimizes the
 552 term-wise distance: $\inf_{\pi} \left(\frac{1}{30} \sum_{i=1}^{30} \|X_i - Y_{\pi(i)}\|^2 \right)^{\frac{1}{2}}$. This allows for the comparison of en-
 553 semble simulations for a given statistic. Tables 2 and 3 (summarized in Figure 11, (a))
 554 provide the *relative distance to LU*. A reference is calculated by taking the Wasserstein
 555 distance between the first 15 and the last 15 members of the same ensemble from the ‘LU’
 556 experiment (for a given turbulent statistic). The *relative distance to LU* is the Wasserstein
 557 distance between two ensembles divided by the latter reference. It can be understood as the
 558 member-to-member distance divided by the distance between members of the LU ensemble.

559 Figure 11 presents the relative distance to LU for each standardized moments of u and
 560 q , gathered on radar charts. The left panel (a) is a summary of Tables 2 and 3 where the
 561 moments take into account the whole computational domain. Conversely, the moments are
 562 computed only on an area around the jet to create the right panel (b). Those radar charts
 563 are in line with the previous conclusions: the statistics of the “Perturbed points” ensemble
 564 are indeed close to those of the “LU” ensemble. All methods introducing a stochastic noise
 565 are closer to LU than the deterministic simulation, with the exception of the “Perturbed
 566 steps” method, due to its systematic creation of vorticity. The latter remark does not apply
 567 as strongly when the moments are computed only in the vicinity of the jet. Finally, we also
 568 note that the relative difference to LU is often less than 1. This means that the variability
 569 of the LU ensemble for those moments is larger than the difference between the studied
 570 approaches.

571 5 Conclusion

572 5.1 Summary

573 This paper has presented a Stochastic Grid Perturbation method based on autoregres-
 574 sive processes that is equivalent to an explicit implementation of the LU method. To achieve

	Deterministic	Perturbed points	Without compensation	Perturbed steps
MEAN	1.502	0.048	1.730	0.074
STD	2.272	0.155	4.436	0.416
SKEWNESS	33.139	0.471	5.772	0.738
KURTOSIS	92.389	0.420	1.435	0.567

Table 2. Relative distance to LU for the velocity u .

	Deterministic	Perturbed points	Without compensation	Perturbed steps
MEAN	0.168	1.466	0.293	643.695
STD	7.442	0.005	7.423	0.056
SKEWNESS	0.746	0.040	0.172	0.907
KURTOSIS	1.581	0.012	0.771	0.098

Table 3. Relative distance to LU for the vorticity q .

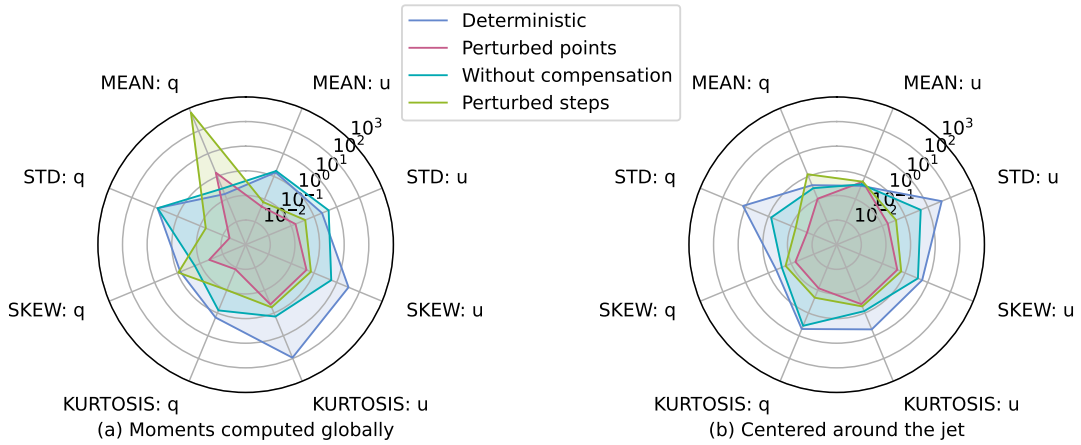


Figure 11. Log scaled radar chart showing the relative distance to LU for the first four standardized moments of the variables u and q . Left panel (a): summary of Tables 2 and 3: the standardized moments are computed on the whole computational domain. Right panel (b): additional analysis where the standardized moments are computed on a smaller portion of the domain, including the jet area.

575 strict equivalence, a compensation term has been added in the form of advection. The im-
 576 portance of this compensation has been numerically studied, and the validity of the grid
 577 perturbation method has been confirmed. Perturbing grid steps differs from perturbing grid
 578 points: transitioning between the two is akin to modifying the operator σ fundamentally,
 579 altering the statistical characteristics of the solutions.

580 In the model employed here, the stochastic transport operator applied to q was a
 581 significant choice. As it was mentioned in Section 3.3, considering velocity u as a prognostic
 582 variable under LU assumptions results in a system with distinct properties. It has been
 583 shown that, with the presence of a stochastic right-hand side, the effect of grid perturbation
 584 can differ from the stochastic transport operator although a numerical estimation hints that
 585 this difference may be small for the Quasi-Geostrophic equations.

586 This paper addresses the link between LU and SGP by modifying the SGP method to
 587 make it similar to LU. This approach is quite natural because LU offers more theoretical
 588 guarantees such as energy conservation along trajectories. However, one could alternatively
 589 design a noise term $\sigma d\mathbf{B}_t$ to express the SGP method as an instance of LU and study its
 590 properties. This noise would feature a Girsanov drift based on its past trajectory. Investi-
 591 gating such a noise within the LU framework would be interesting but challenging.

592 5.2 Application scenarios and limitations of SGP

593 The starting point of this study is the implementation of SGP in NEMO (Leroux et
 594 al., 2022). This implementation was motivated by the apparent simplicity of perturbing the
 595 grid to control the spread of an ensemble. However, their goal was not to implement exactly
 596 a LU method and the noise introduced was homogeneous. Indeed, the main difficulty of
 597 most LU implementations is the parameterization of the operator σ . This can be achieved
 598 for instance through offline analysis of high-resolution simulations based on Empirical Or-
 599 thogonal Functions (Tucciarone et al., 2023) or more elaborate approach (Tucciarone et al.,
 600 2024).

601 When the SGP described in this paper is integrated into an Eulerian code with the
 602 compensation term, it combines the stochastic Eulerian transport of the compensation term
 603 with grid perturbation. In contrast, explicitly implementing LU would solely necessitate a
 604 stochastic Eulerian transport.

605 On another hand, there is presently an emerging interest in the use of Arbitrary La-
 606 grangian Eulerian (ALE) methods (e.g. (Donea et al., 2004)) in the ocean modelling com-
 607 munity. In such a perspective, it is interesting to note that within a code built upon an
 608 ALE framework, grid points can undergo direct perturbation using $\sigma d\mathbf{B}_t$ without the need
 609 for Ornstein-Uhlenbeck processes and a compensation term.

610 Applying the SGP method amounts to treat the smooth component of the motion in
 611 an Eulerian manner while using a Lagrangian method for the uncorrelated motion. This is
 612 somewhat similar to the so-called fractional-step methods (e.g. Huerta & Casadei, 1994),
 613 widely used in ALE frameworks. Therefore, this study presents the option of a semi-
 614 Lagrangian implementation of the LU equations, which holds more significance for semi-
 615 Lagrangian frameworks. Future work could focus on adapting this semi-Lagrangian setting
 616 to other discretization methods, such as Finite Volume methods.

617 Open Research Section

618 The numerical model, the code for statistical analyses and the code generating the
 619 Figures and Tables can be found in the repository “Stochastic Grid Perturbation” (Clement
 620 & Li, 2024) at address https://gricad-gitlab.univ-grenoble-alpes.fr/clemensi/qgm_sgp.
 621 The latter Python3.10 code is under MIT license. Moreover, the datasets containing

622 the outputs of the simulations used in the Figures are available in Zenodo (Clement, 2024)
 623 at <https://doi.org/10.5281/zenodo.11650897>.

624 Acknowledgments

625 Parts of the computations presented in this paper were performed using the GRICAD infras-
 626 tructure (<https://gricad.univ-grenoble-alpes.fr>), which is supported by Grenoble research
 627 communities. This work was supported by funding from the French government through
 628 the National Research Agency as part of France 2030, under references ANR-22-POCE-0003
 629 and ANR-19-CE46-0011. L.L. and E.M. acknowledge the support of the ERC EU project
 630 856408-STUOD.

631 References

- 632 Bauer, W., Chandramouli, P., Chapron, B., Li, L., & Mémin, E. (2020a). Deciphering
 633 the role of small-scale inhomogeneity on geophysical flow structuration: a stochastic
 634 approach. *Journal of Physical Oceanography*, *50*(4), 983–1003.
- 635 Bauer, W., Chandramouli, P., Li, L., & Mémin, E. (2020b). Stochastic representation of
 636 mesoscale eddy effects in coarse-resolution barotropic models. *Ocean Modelling*, *151*,
 637 101646.
- 638 Berner, J., Achatz, U., Batté, L., Bengtsson, L., Cámara, A., Christensen, H., ... others
 639 (2017). Stochastic parameterization: Toward a new view of weather and climate
 640 models. *Bulletin of the American Meteorological Society*, *98*(3), 565–588.
- 641 Brecht, R., Li, L., Bauer, W., & Mémin, E. (2021). Rotating shallow water flow under
 642 location uncertainty with a structure-preserving discretization. *Journal of Advances
 643 in Modeling Earth Systems*, *13*(12), e2021MS002492.
- 644 Chapron, B., Dérian, P., Mémin, E., & Resseguier, V. (2018). Large-scale flows under
 645 location uncertainty: a consistent stochastic framework. *QJRM*, *144*(710), 251–260.
- 646 Clement, S. (2024). *Data of the Stochastic Grid Perturbation comparison with Location
 647 Uncertainty framework*. Zenodo. doi: 10.5281/zenodo.11654106
- 648 Clement, S., & Li, L. (2024). *Stochastic Grid Perturbation on Quasi-Geostrophic model*.
 649 Retrieved from <https://hal.science/hal-04611878>
- 650 Crisan, D., Flandoli, F., & Holm, D. (2019). Solution properties of a 3D stochastic Euler
 651 fluid equation. *Journal of Nonlinear Science*, *29*(3), 813–870.
- 652 Debussche, A., Hug, B., & Mémin, E. (2023). A consistent stochastic large-scale representa-
 653 tion of the navier–stokes equations. *Journal of Mathematical Fluid Mechanics*, *25*(1),
 654 19. doi: 10.1007/s00021-023-00764-0
- 655 Debussche, A., & Mémin, E. (2024). Variational principles for fully coupled stochastic fluid
 656 dynamics across scales. *ArXiv*(2409.12654).
- 657 Donea, J., Huerta, A., Ponthot, J.-P., & Rodriguez-Ferran, A. (2004). Arbitrary lagrangian
 658 eulerian methods. In *Encyclopedia of computational mechanics* (chap. 14). John Wiley
 659 & Sons, Ltd. doi: 10.1002/0470091355.ecm009
- 660 Falkovich, G., Gawedzki, K., & Vergassola, M. (2001). Particles and fields in fluid turbulence.
 661 *Rev. Mod. Phys.*, *73*, 913–975. doi: 10.1103/RevModPhys.73.913
- 662 Fedrizzi, E., & Flandoli, F. (2013). Noise prevents singularities in linear transport equations.
 663 *Journal of Functional Analysis*, *264*(6), 1329–1354. doi: [https://doi.org/10.1016/
 664 j.jfa.2013.01.003](https://doi.org/10.1016/j.jfa.2013.01.003)
- 665 Gawedzky, K., & Kupiainen, A. (1995). Anomalous scaling of the passive scalar. *Physical
 666 review letters*, *75*, 3834–3837.
- 667 Gottwald, G., Crommelin, D., & Franzke, C. (2017). Stochastic climate theory. In *Nonlinear
 668 and stochastic climate dynamics* (p. 209–240). Cambridge University Press.
- 669 Hasselmann, K. (1976, 2024/06/25). Stochastic climate models Part I. Theory. *Tellus*,
 670 *28*(6), 473–485.
- 671 Hogg, A. M. C., Killworth, P. D., Blundell, J. R., & Dewar, W. K. (2005). Mechanisms of
 672 decadal variability of the wind-driven ocean circulation. *Journal of Physical Oceanog-*

- 673 raphy, 35(4), 512–531.
- 674 Holm, D. D. (2015). Variational principles for stochastic fluid dynamics. *Proceedings of*
675 *the Royal Society A: Mathematical, Physical and Engineering Sciences*, 471(2176),
676 20140963.
- 677 Huerta, A., & Casadei, F. (1994). New ALE applications in non-linear fast-transient solid
678 dynamics. *Engineering Computations*, 11(4), 317–345.
- 679 Kitsios, V., Frederiksen, J. S., & O’Kane, T. J. (2023). Subgrid parameterization of
680 eddy, meanfield and topographic interactions in simulations of an idealized antarctic
681 circumpolar current. *Journal of Advances in Modeling Earth Systems*, 15(5),
682 e2022MS003412. doi: 10.1029/2022MS003412
- 683 Kraichnan, R. (1959). The structure of isotropic turbulence at very high reynolds numbers.
684 *J. of Fluids Mech.*, 5, 477–543.
- 685 Kraichnan, R. (1994). Anomalous scaling of a randomly advected passive scalar. *Physical*
686 *Review Letters*, 72(7), 1016.
- 687 Kunita, H. (1990). *Stochastic flows and stochastic differential equations* (Vol. 24). Cam-
688 bridge university press.
- 689 Lang, O., Crisan, D., & Mémin, E. (2023). Analytical properties for a stochastic rotat-
690 ing shallow water model under location uncertainty. *Journal of Mathematical Fluid*
691 *Mechanics*, 25(2), 29. doi: 10.1007/s00021-023-00769-9
- 692 Leith, C. (1990). Stochastic backscatter in a subgrid-scale model: plane shear mixing layer.
693 *Phys. of Fluids*, 2(3), 1521–1530.
- 694 Leroux, S., Brankart, J.-M., Albert, A., Brodeau, L., Molines, J.-M., Jamet, Q., ...
695 Brasseur, P. (2022). Ensemble quantification of short-term predictability of the ocean
696 dynamics at a kilometric-scale resolution: a Western Mediterranean test case. *Ocean*
697 *Science*, 18(6), 1619–1644.
- 698 Lesieur, M., & Métais, O. (1996). New trends in large-eddies simulation of turbulence.
699 *Annu. Rev. Fluid. Mech.*, 28, 45–82.
- 700 Li, L. (2021). *Stochastic modeling and numerical simulation of ocean dynamics* (Unpublished
701 doctoral dissertation). Université de Rennes 1.
- 702 Li, L., Deremble, B., Lahaye, N., & Mémin, E. (2023a). Stochastic Data-Driven Parameter-
703 ization of Unresolved Eddy Effects in a Baroclinic Quasi-Geostrophic Model. *Journal*
704 *of Advances in Modeling Earth Systems*, 15(2), e2022MS003297.
- 705 Li, L., Mémin, E., & Tissot, G. (2023b). Stochastic parameterization with dynamic mode
706 decomposition. In B. Chapron, D. Crisan, D. Holm, E. Mémin, & A. Radomska
707 (Eds.), *Stochastic transport in upper ocean dynamics* (pp. 179–193). Cham: Springer
708 International Publishing.
- 709 Majda, A., & Kramer, P. (1999). Simplified models for turbulent diffusion: theory, numerical
710 modelling, and physical phenomena. *Physics report*, 314, 237–574.
- 711 Mason, P., & Thomson, D. (1992). Stochastic backscatter in large-eddy simulations of
712 boundary layers. *J. of Fluid Mech.*, 242, 51–78.
- 713 Mémin, E., Li, L., Lahaye, N., Tissot, G., & Chapron, B. (2024). Linear wave solutions of
714 a stochastic shallow water model. In *Stochastic transport in upper ocean dynamics ii*
715 (pp. 223–245). Springer International Publishing.
- 716 Mémin, E. (2014). Fluid flow dynamics under location uncertainty. *Geophysical & Astro-*
717 *physical Fluid Dynamics*, 108(2), 119–146.
- 718 O’Kane, T. J., Fiedler, R., Collier, M. A., & Kitsios, V. (2023). Ocean model response to
719 stochastically perturbed momentum fluxes. *Journal of Climate*, 36(6), 1895–1922.
- 720 Resseguier, V., Mémin, E., & Chapron, B. (2017a). Geophysical flows under location un-
721 certainty, Part I Random transport and general models. *Geophysical & Astrophysical*
722 *Fluid Dynamics*, 111(3), 149–176.
- 723 Resseguier, V., Mémin, E., & Chapron, B. (2017b). Geophysical flows under location
724 uncertainty, Part II Quasi-geostrophy and efficient ensemble spreading. *Geophysical*
725 *& Astrophysical Fluid Dynamics*, 111(3), 177–208.
- 726 Thiry, L., Li, L., & Mémin, E. (2023). Modified (hyper-)viscosity for coarse-resolution
727 ocean models. In B. Chapron, D. Crisan, D. Holm, E. Mémin, & A. Radomska (Eds.),

- 728 *Stochastic transport in upper ocean dynamics* (pp. 273–285). Cham: Springer Inter-
729 national Publishing.
- 730 Tucciarone, F. L., Mémin, E., & Li, L. (2023). Primitive equations under location uncer-
731 tainty: Analytical description and model development. In B. Chapron, D. Crisan,
732 D. Holm, E. Mémin, & A. Radomska (Eds.), *Stochastic transport in upper ocean dy-*
733 *namics* (pp. 287–300). Cham: Springer International Publishing.
- 734 Tucciarone, F. L., Mémin, E., & Li, L. (2024). Data driven stochastic primitive equations
735 with dynamic modes decomposition. In B. Chapron, D. Crisan, D. Holm, E. Mémin,
736 & A. Radomska (Eds.), *Stochastic transport in upper ocean dynamics ii* (pp. 321–336).
737 Cham: Springer Nature Switzerland.
- 738 Zhen, Y., Resseguier, V., & Chapron, B. (2023). Physically constrained covariance inflation
739 from location uncertainty. *Nonlinear Processes in Geophysics*, *30*(2), 237–251.